

User-Assisted Approach for Accurate Nonrigid Registration of Images and Traces

Mirza M. Junaid Baig[1,2(✉)], Tina Thuy N. Hoang[2], Samuel H. Chung[2], and Armen Stepanyants[1]

[1] Department of Physics, Northeastern University, Boston, MA 02115, USA
{baig.mi,a.stepanyants}@northeastern.edu
[2] Department of Bioengineering, Northeastern University, Boston, MA 02115, USA

Abstract. Registration—the process of aligning datasets into a common coordinate system—is a fundamental part of many medical, scientific, and engineering applications. While automated algorithms are widely used for this task, they are often prone to getting trapped in local minima of their objective functions, resulting in alignment errors that are easy to detect but difficult to correct. Traditional solutions often involve iterative parameter tuning, data preprocessing and preregistering, and multiple algorithm reruns—an approach that is both time-consuming and does not guarantee satisfactory results. Therefore, for tasks where registration accuracy is more important than speed, it is appropriate to explore alternative, user-assisted registration strategies. In such tasks, finding and correcting errors in automated registration is often more time-consuming than directly integrating user input during the registration process.

Therefore, this study evaluates a user-assisted approach for accurate nonrigid registration of images and traces. By leveraging the corresponding sets of fiducial points provided by the user to guide the registration, the algorithm computes an optimal nonrigid transformation that combines linear and nonlinear components. Our findings demonstrate that the registration accuracy of this approach improves consistently with the increased complexity of the linear transformation and as more fiducial points are provided, while the results compare favorably to standard registration methods. Consequently, accuracy sufficient for many biomedical applications can be achieved within minutes, requiring only a small number of user-provided fiducial points.

Keywords: Registration · Affine · Nonrigid · Point Sets · Coherent Point Drift · Fiducial Points · Key Points

1 Introduction

Registration involves aligning one or more datasets to a common coordinate system, enabling quantitative comparisons and meaningful combinations of data. It is essential for detecting changes in longitudinal studies [1, 2], performing cross-subject comparisons [3], and integrating multimodal data [4, 5]. As such, registration is a fundamental tool in computer vision [6, 7], as well as biological [8] and medical [9, 10] applications.

© The Author(s), under exclusive license to Springer Nature Switzerland AG 2026
O. Gervasi et al. (Eds.): ICCSA 2025 Workshops, LNCS 15892, pp. 345–357, 2026.
https://doi.org/10.1007/978-3-031-97638-4_22

However, despite its broad applicability, registration remains a challenging problem, particularly in a nonrigid setting. Fully automated algorithms offer efficiency but can struggle with large rotations and deformations, high structural variability, and experimental artifacts [11]. Such methods usually rely on simplistic models that can get trapped in local minima of their objective functions, leading to erroneous solutions. For instance, even state-of-the-art fully automated algorithms for point set registration such as Coherent Point Drift (CPD) [12, 13] and Bayesian Coherent Point Drift (BCPD) [14] are prone to such problems (Fig. 1A). Preregistering the data can improve the outcome but often falls short of achieving satisfactory results (Fig. 1B). Extensive parameter tuning may improve performance but undermines the goal of full automation.

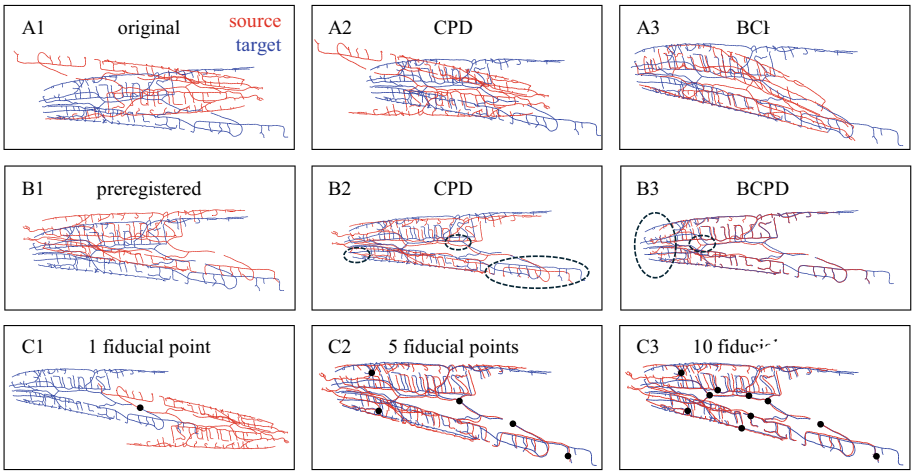

Fig. 1. User-assisted registration circumvents problems associated with fully automated algorithms. **A.** Fully automated registration often converges to suboptimal solutions. This is illustrated through the registration of 3D traces of FLP neurons using CPD and BCPD algorithms with default parameters. **B.** After the user preregisters the traces, performance improves but does not yield satisfactory results (circled regions). **C.** User-assisted registration gradually improves with an increasing number of user-defined fiducial points, leading to a superior result.

Instead, user-assisted methods can provide more efficient and reliable alternatives from the start. In such methods, expert users provide key corresponding landmarks, addressing many challenges of full automation by prioritizing accuracy over speed. The accuracy of user-assisted methods depends on user experience and effort (Fig. 1C), and the desired outcome can be achieved in any application given a suitable registration model. Therefore, such methods can yield superior performance, making them well-suited for complex biomedical applications. Existing tools employ various mathematical models to achieve registration, each with its strengths and limitations. For instance, the widely used 3D Slicer software [15] can use Thin-Plate Spline [16] to smoothly interpolate across deformations between corresponding landmarks, making it effective for applications requiring smooth global warping. Another popular application, BUnwarpJ [17], uses B-spline for registration, allowing greater control for local deformations but

requiring a carefully chosen grid resolution. In contrast, the method presented in this study exactly registers user-defined fiducial points with a hybrid linear-nonlinear model, allowing both smooth global transformations and local refinements.

Many recent advances in registration have been driven by Deep Learning (DL) [18]. Techniques such as Reinforcement Learning [19, 20] and Generative Adversarial Networks [19, 21, 22] have demonstrated impressive improvements in accuracy and robustness. The power of DL-based methods lies in their ability to generalize across datasets and achieve good results without direct user involvement once the model is created. However, DL-based methods require extensive training datasets which are arduous to create and incur high computational costs. In addition, their reliance on black-box models that lack interpretability makes it difficult to address domain-specific constraints to ensure meaningful outcomes [19, 23]. Thus, while DL-based methods have a significant potential for advancing the field of registration, at present, they are not the best fit for biomedical applications where accuracy, interpretability, and flexibility are paramount.

The user-assisted registration approach presented in this study offers a complementary solution that combines user expertise with algorithmic efficiency, enabling high accuracy while preserving interpretability. The specific contributions of this study include the following: (1) The registration problem is formulated as an exactly solvable model that combines linear and nonlinear transformations to achieve an exact registration of user-defined fiducial points. (2) Four types of linear transformations are considered within a single framework: translation, rigid, similarity, and affine. (3) A novel treatment of linear transformations is introduced in which an optimal rotation is discounted from the objective function. This enables the formulation and testing of a hypothesis that increasing the complexity of the linear transformation can minimize the warping of the space.

The proposed approach supports the registration of 2D and 3D point sets, traces, and images. It includes a graphical interface that enables users to visually select corresponding fiducial points and iteratively refine the registration outcome (Fig. 1C). This is particularly useful for domain scientists working with specialized datasets for which there are no immediate registration solutions available. By leveraging expert input and focusing on interpretability, the method provides a reliable alternative to DL-based techniques, particularly in applications that require domain-specific precision and flexibility. The utility of this approach is demonstrated through the registration of 3D traces of *C. elegans* neurons and 2D images of the human retina, showing significant improvements in accuracy over fully automated methods.

The remainder of this paper is organized as follows. Section 2 formulates the model of the exact registration of fiducial points with a combination of linear and CPD-based nonlinear transformations. In Sect. 3, the model is solved analytically by using standard methods from constrained optimization and calculus of variations. In Sect. 4, the solution is illustrated on the task of registering synthetic images, and in Sect. 5, the performance of the registration method is evaluated on two biomedical datasets. Section 6 contains a summary and brief discussion of the results.

2 Model for Exact Registration of Fiducial Points with a Combination of Linear and Nonlinear Transformations

Consider point sets X, referred to as the source, and Y, referred to as the target, in $\mathbb{R}^D$ containing N user-defined fiducial points each (Fig. 2A). Positions of the points are denoted with vectors $\mathbf{x}_i$ and $\mathbf{y}_i$ respectively ($i = 1, \ldots, N$), and their correspondences are known. The point set X must be transformed and registered to Y, which remains fixed. The registering transformation, $\mathbf{T}(\mathbf{x}) = \mathbf{A}\mathbf{x} + \mathbf{b} + \mathbf{V}(\mathbf{x})$, which consists of a linear component governed by matrix $\mathbf{A}$ and vector $\mathbf{b}$, and a nonlinear part described by a vector-valued function $\mathbf{V}(\mathbf{x})$, must match the corresponding fiducial points exactly, i.e., $\mathbf{y}_i = \mathbf{T}(\mathbf{x}_i) = \mathbf{A}\mathbf{x}_i + \mathbf{b} + \mathbf{V}(\mathbf{x}_i)$ for all i (Fig. 2A). The nonlinear part of the registering transformation is modeled with the Coherent Point Drift (CPD) method of Myronenko et al. [13], and the following four types of linear transformations of increasing complexity are considered:

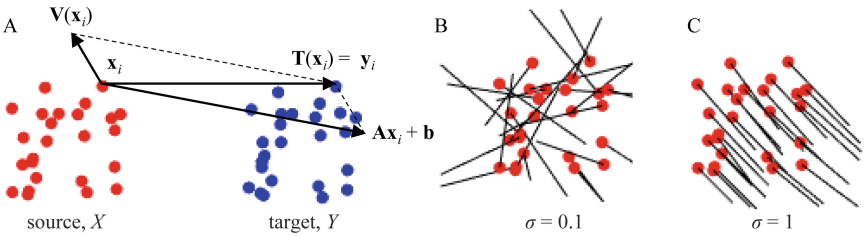

Fig. 2. Registering transformation. **A.** Source and target point sets with known correspondences before registration. The sum of displacement vectors for linear and nonlinear parts of the registering transformation for each source point ($\mathbf{x}_i$) results in a displacement that exactly matches the position of the corresponding target point ($\mathbf{y}_i$). **B.** Nonlinear displacement field of the source points, $\mathbf{V}(\mathbf{x}_i)$, is indicated with black lines. **C.** Coherence of the nonlinear displacement field increases with σ. Point set X was randomly drawn from a unit cube and Y was generated from X by adding random displacements in the $[-0.1\ 0.1]$ range. Registration was performed with an affine + nonlinear transformation with $\lambda = 0$.

$$\begin{aligned} &\text{Translation}: \quad \mathbf{A} = \mathbf{I}_D \\ &\text{Rigid}: \quad \mathbf{A}^T\mathbf{A} = \mathbf{I}_D, \quad \det(\mathbf{A}) = 1 \\ &\text{Similarity}: \quad \mathbf{A}^T\mathbf{A} = s^2\mathbf{I}_D, \quad \det(\mathbf{A}) > 0, \quad s > 0 \\ &\text{Affine}: \quad \mathbf{A} \in \mathbb{R}^{D\times D}. \end{aligned} \tag{1}$$

In these expressions and below, bold lower-case letters represent $D \times 1$ vectors, bold upper-case characters denote $D \times D$ matrices, or, in the cases of $\mathbf{T}(\mathbf{x})$ and $\mathbf{V}(\mathbf{x})$, $D \times 1$ vector-valued functions. The trace of a matrix is denoted as tr and $\mathbf{I}_D$ represents a $D \times D$ identity matrix. In the similarity case, $\mathbf{A}$ can be written as a product of a uniform scaling factor s and a rotation matrix.

Parameters of the registering transformation are determined through the minimization of the heuristic cost of space deformation associated with the nonrigid nature of

$\mathbf{T}(\mathbf{x})$, subject to constraints on this transformation:

$$\begin{aligned}(\hat{\mathbf{A}}, \hat{\mathbf{R}}, \hat{\mathbf{b}}, \hat{\mathbf{V}}) = \underset{\mathbf{A},\mathbf{R},s,\mathbf{b},\mathbf{V}}{\arg\min} \left\{ \frac{\lambda}{E_L^{norm}} \|\mathbf{A} - \mathbf{R}\|_F^2 + \frac{1-\lambda}{E_N^{norm}} \int \frac{|\tilde{\mathbf{V}}(\mathbf{k})|^2}{\tilde{G}(\mathbf{k})} \frac{d^D\mathbf{k}}{(2\pi)^D} \right\}, \quad 0 \le \lambda < 1 \\ \text{s.t.} \quad \mathbf{R}^T\mathbf{R} = \mathbf{I}_D, \quad \det(\mathbf{R}) = 1 \\ \text{Eq.(1) constraints on } \mathbf{A} \\ \mathbf{A}\mathbf{x}_i + \mathbf{b} + \mathbf{V}(\mathbf{x}_i) = \mathbf{y}_i, \quad i = 1, \ldots, N.\end{aligned} \tag{2}$$

The heuristic cost of Eq. (2) is a weighted sum of normalized costs associated with the linear (E_L) and nonlinear (E_N) deformations induced by $\mathbf{T}(\mathbf{x})$. Parameter λ shifts the balance of these contributions from a purely nonlinear cost at $\lambda = 0$ to a purely linear cost in the $\lambda \to 1$ limit. The linear cost component is a normalized squared Frobenius norm of the difference between $\mathbf{A}$ and an orthogonal matrix with unit determinant, $\mathbf{R}$ (rotation without reflection). The latter matrix is determined during optimization and ensures that an optimal rotation is discounted from the linear deformation cost. The nonlinear cost component is a normalized CPD metric [13], where $\tilde{\mathbf{V}}(\mathbf{k})$ represents a Fourier transform of $\mathbf{V}(\mathbf{x})$ and $\tilde{G}(\mathbf{k})$ denotes a Fourier transform of a Gaussian function

$$G(\mathbf{x}) = \left(2\pi\sigma^2\right)^{\frac{-D}{2}} e^{\frac{-1}{2\sigma^2}\mathbf{x}^T\mathbf{x}}, \quad \tilde{G}(\mathbf{k}) = e^{\frac{-\sigma^2}{2}\mathbf{k}^T\mathbf{k}}. \tag{3}$$

Parameter σ is referred to as the coherence parameter, for the reason that the structure of the nonlinear cost component forces the source points that are within distance σ of each other to move coherently (in similar directions) during the transformation [13] (Fig. 2B, C).

The normalization factors for the linear and nonlinear cost components, E_L^{norm} and E_N^{norm} in Eq. (2) are included to ensure that the two cost terms have similar scales, making it easier to interpret the tradeoffs of their contributions. These normalization factors will be deduced following the solution of the optimization problem and will depend on the positions of the source and target points and the coherence parameter, but not on λ and the type of linear transformation. This will enable comparisons of registration results when different transformations are applied to the same point sets.

The described registration model is governed by only two parameters, λ and σ, and the outcome of registration depends on the choice of the linear transformation and fiducial points provided by the user.

3 Solution of the Model

The heuristic cost of Eq. (2) must be minimized with respect to variables $\mathbf{A}$, $\mathbf{R}$, s (similarity only), $\mathbf{b}$, and function $\mathbf{V}(\mathbf{x})$, subject to constraints. This is done gradually starting with the optimization of function $\mathbf{V}(\mathbf{x})$. To that end, the third set of constraints of Eq. (2) is included in the heuristic cost using Lagrange multipliers $\mathbf{c}_i$,

$$\begin{aligned}\hat{\mathbf{V}} = \underset{\mathbf{V}}{\arg\min} \left\{ \frac{\lambda}{E_L^{norm}} \|\mathbf{A} - \mathbf{R}\|_F^2 + \frac{1-\lambda}{E_N^{norm}} \int \frac{|\tilde{\mathbf{V}}(\mathbf{k})|^2}{\tilde{G}(\mathbf{k})} \frac{d^D\mathbf{k}}{(2\pi)^D} + \right. \\ \left. \frac{1-\lambda}{N} \sum_{i=1}^{N} \mathbf{c}_i^T \left(\mathbf{A}\mathbf{x}_i + \mathbf{b} + \mathbf{V}(\mathbf{x}_i) - \mathbf{y}_i\right) \right\},\end{aligned} \tag{4}$$

and the optimization is performed with standard methods of variational calculus [24]. The result shows that $\hat{\mathbf{V}}$ is a mixture of Gaussians, and the Lagrange multipliers $\mathbf{c}_i$ depend on the inverse of the Gaussian kernel, $\mathcal{G} = \{G(\mathbf{x}_i - \mathbf{x}_j)\} \in \mathbb{R}^{N \times N}$:

$$\begin{aligned} \hat{\mathbf{V}}(\mathbf{x}) &= \tfrac{-E_N^{norm}}{2N} \sum_{i=1}^{N} \mathbf{c}_i G(\mathbf{x} - \mathbf{x}_i) \\ \mathbf{c}_i &= \tfrac{2N}{E_N^{norm}} \sum_{j=1}^{N} \left(\mathcal{G}^{-1}\right)_{i,j} \left(\mathbf{A}\mathbf{x}_j + \mathbf{b} - \mathbf{y}_j\right), \quad i = 1, \ldots, N. \end{aligned} \tag{5}$$

Next, after eliminating $\hat{\mathbf{V}}$ from the original optimization problem of Eq. (2), the process is continued by performing minimization with respect to $\mathbf{b}$. This is done by setting the corresponding gradient of the heuristic cost to zero and solving the resulting equation, which yields

$$\begin{aligned} &\hat{\mathbf{b}} = \arg\min_{\mathbf{b}} \Big\{ \tfrac{\lambda}{E_L^{norm}} \|\mathbf{A} - \mathbf{R}\|_F^2 + \\ &\tfrac{1-\lambda}{E_N^{norm}} \sum_{i,j=1}^{N} \left(\mathcal{G}^{-1}\right)_{i,j} \left(\mathbf{A}\mathbf{x}_i + \mathbf{b} - \mathbf{y}_i\right)^T \left(\mathbf{A}\mathbf{x}_j + \mathbf{b} - \mathbf{y}_j\right) \Big\} = -\mathbf{A}\langle \mathbf{x} \rangle_{\mathcal{G}^{-1}} + \langle \mathbf{y} \rangle_{\mathcal{G}^{-1}} \\ &\langle \mathbf{a} \rangle_{\mathcal{G}^{-1}} \equiv \sum_{i,j=1}^{N} \left(\mathcal{G}^{-1}\right)_{i,j} \mathbf{a}_j \Big/ \sum_{i,j=1}^{N} \left(\mathcal{G}^{-1}\right)_{i,j}. \end{aligned} \tag{6}$$

The remaining problem, concisely written with the help of modified covariance matrices $\mathbf{Q}_{pq} = \sum_{i,j=1}^{N} \left(\mathbf{p}_i - \langle \mathbf{p} \rangle_{\mathcal{G}^{-1}}\right) \left(\mathcal{G}^{-1}\right)_{i,j} \left(\mathbf{q}_j - \langle \mathbf{q} \rangle_{\mathcal{G}^{-1}}\right)^T$, is

$$\begin{aligned} \left(\hat{\mathbf{A}}, \hat{\mathbf{R}}\right) &= \arg\min_{\mathbf{A},\mathbf{R},s} \Big\{ \tfrac{\lambda}{E_L^{norm}} \|\mathbf{A} - \mathbf{R}\|_F^2 + \tfrac{1-\lambda}{E_N^{norm}} \mathrm{tr}\left(\mathbf{A}\mathbf{Q}_{xx}\mathbf{A}^T - 2\mathbf{A}\mathbf{Q}_{xy} + \mathbf{Q}_{yy}\right) \Big\} \\ &\text{s.t.} \quad \mathbf{R}^T\mathbf{R} = \mathbf{I}_D, \quad \det(\mathbf{R}) = 1. \end{aligned} \tag{7}$$

This problem is solved by employing the singular value decomposition (SVD) trick [25], which helps to enforce the constraints on matrix $\mathbf{R}$. The results for the four types of linear transformations are summarized in Table 1.

The solution for each type of linear transformation must be constructed by executing the rows of Table 1 from top to bottom. Matrix $\mathbf{I}'_D$ which appears in the expressions for $\hat{\mathbf{R}}$ is the identity matrix $\mathbf{I}_D$ with 1 in the last row and column replaced with $\det(\mathbf{V}\mathbf{U}^T)$. The nonlinear part of the registering transformation ensures that, so long as points in set X are in general positions, any registration problem is feasible, i.e. an optimal solution satisfying the constraints of Eq. (2) can be found. The coherence of the nonlinear displacement field, $\mathbf{V}(\mathbf{x})$, is governed by parameter σ, such that points within σ move in similar directions, Eq. (5) (Fig. 2B, C).

Equation (7) shows that the normalized costs of linear and nonlinear deformations, E_L and E_N, calculated based on the optimal transformation are

$$\begin{aligned} E_L &= \tfrac{1}{E_L^{norm}} \left\|\hat{\mathbf{A}} - \hat{\mathbf{R}}\right\|_F^2 \\ E_N &= \tfrac{1}{E_N^{norm}} \mathrm{tr}\left(\hat{\mathbf{A}}\mathbf{Q}_{xx}\hat{\mathbf{A}}^T - 2\hat{\mathbf{A}}\mathbf{Q}_{xy} + \mathbf{Q}_{yy}\right). \end{aligned} \tag{8}$$

Table 1. Model solutions for the considered linear transformation types.

	Translation	Rigid	Similarity	Affine
SVD	–	$\mathbf{Q}_{xy} = \mathbf{U}\mathbf{\Sigma}\mathbf{V}^T$		$\left(\frac{\lambda}{E_L^{norm}}\mathbf{I}_D + \frac{1-\lambda}{E_N^{norm}}\mathbf{Q}_{xx}\right)^{-1}\mathbf{Q}_{xy} = \mathbf{U}\mathbf{\Sigma}\mathbf{V}^T$
$\hat{\mathbf{R}}$	$\mathbf{I}_D$	$\mathbf{V}\mathbf{I}'_D\mathbf{U}^T$		
$\hat{\mathbf{A}}$	$\hat{\mathbf{R}}$		$\frac{\frac{\lambda}{E_L^{norm}}D + \frac{1-\lambda}{E_N^{norm}}\mathrm{tr}(\hat{\mathbf{R}}\mathbf{Q}_{xy})}{\frac{\lambda}{E_L^{norm}}D + \frac{1-\lambda}{E_N^{norm}}\mathrm{tr}(\mathbf{Q}_{xx})}\hat{\mathbf{R}}$	$\left(\frac{\lambda}{E_L^{norm}}\hat{\mathbf{R}} + \frac{1-\lambda}{E_N^{norm}}\mathbf{Q}_{yx}\right)\times \left(\frac{\lambda}{E_L^{norm}}\mathbf{I}_D + \frac{1-\lambda}{E_N^{norm}}\mathbf{Q}_{xx}\right)^{-1}$
$\hat{\mathbf{b}}$	$-\hat{\mathbf{A}}\langle\mathbf{x}\rangle_{\mathcal{G}^{-1}} + \langle\mathbf{y}\rangle_{\mathcal{G}^{-1}}$			
$\hat{\mathbf{V}}(\mathbf{x})$	$-\sum_{i,j=1}^{N} G(\mathbf{x}-\mathbf{x}_i)\left(\mathcal{G}^{-1}\right)_{i,j}\left(\hat{\mathbf{A}}\mathbf{x}_j + \hat{\mathbf{b}} - \mathbf{y}_j\right)$			

It remains to determine the normalization factors E_L^{norm} and E_N^{norm} to ensure that, for the given σ and point sets, E_L and E_N as functions of λ have similar bounds for all linear transformation types.

To accomplish this, we examine the dependence of these cost components on λ. When $\lambda = 0$, the burden of registration is placed maximally on the linear transformation because it incurs no penalty. Therefore, the maximal E_L is expected at $\lambda = 0$ for all linear transformation types. Similarly, in the $\lambda \to 1$ limit, the nonlinear part of the transformation does not contribute to the heuristic cost of Eq. (2) and is expected to cause the largest spatial distortion resulting in a maximal E_N. This reasoning is confirmed by direct analytical calculations, and an example of the dependence of the normalized cost components on λ is shown in Fig. 3C. Therefore, we focus on these limiting cases and show the explicit expressions for E_L at $\lambda = 0$ and E_N at $\lambda \to 1$ for all linear transformation types (Table 2).

Because the affine transformation is more flexible than the rest, it usually incurs a higher cost (see Fig. 3C for an example). E_L^{norm} is chosen to make the normalized cost of this transformation equal to 1 at $\lambda = 0$. On the other hand, because translation is the simplest of the considered transformations, it is accompanied by the largest nonlinear deformation, and E_N^{norm} is set in a way that makes the normalized cost of this deformation equal to 1. Therefore,

$$\begin{aligned} E_L^{norm} &= \mathrm{tr}\left(\left(\mathbf{I}'_D - \mathbf{\Sigma}\right)^2\right), \quad \mathbf{Q}_{xx}^{-1}\mathbf{Q}_{xy} = \mathbf{U}\mathbf{\Sigma}\mathbf{V}^T \\ E_N^{norm} &= \mathrm{tr}\left(\mathbf{Q}_{xx} - 2\mathbf{Q}_{xy} + \mathbf{Q}_{yy}\right). \end{aligned} \tag{9}$$

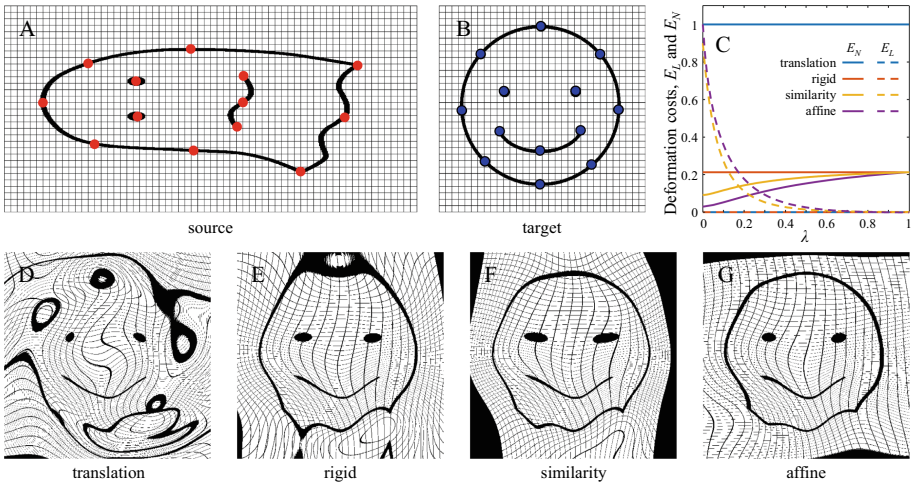

Fig. 3. Increasing the complexity of linear transformation reduces space distortion resulting from registration. **A**: Sample source image with 13 fiducial points marked in red (513 × 1026 pixels). **B**: Target image with the corresponding fiducial points marked in blue (513 × 513 pixels). **C**. Normalized deformation costs associated with the linear (E_L) and nonlinear (E_N) parts of the registering transformation as functions of parameter λ ($\sigma = 75$). **D-G.** Results of registration for the considered transformation types. The fiducial points are registered exactly by all transformations, and the warping of the space decreases systematically from translation to rigid to similarity to affine ($\sigma = 75$ and $\lambda = 0$).

Table 2. Expressions for E_L at $\lambda = 0$ and E_N at $\lambda \to 1$ for the optimal transformations from Table 1.

		Translation	Rigid	Similarity	Affine
$\lambda = 0$	SVD	–	$\mathbf{Q}_{xy} = \mathbf{U}\mathbf{\Sigma}\mathbf{V}^T$		$\mathbf{Q}_{xx}^{-1}\mathbf{Q}_{xy} = \mathbf{U}\mathbf{\Sigma}\mathbf{V}^T$
	E_L	0		$\frac{D}{E_L^{norm}}\left(1 - \frac{\mathrm{tr}(\mathbf{I}'_D\mathbf{\Sigma})}{\mathrm{tr}(\mathbf{Q}_{xx})}\right)^2$	$\frac{\mathrm{tr}\left((\mathbf{I}'_D - \mathbf{\Sigma})^2\right)}{E_L^{norm}}$
$\lambda \to 1$	SVD	–	$\mathbf{Q}_{xy} = \mathbf{U}\mathbf{\Sigma}\mathbf{V}^T$		
	E_N	$\frac{\mathrm{tr}(\mathbf{Q}_{xx} - 2\mathbf{Q}_{xy} + \mathbf{Q}_{yy})}{E_N^{norm}}$	$\frac{\mathrm{tr}(\mathbf{Q}_{xx} - 2\mathbf{I}'_D\mathbf{\Sigma} + \mathbf{Q}_{yy})}{E_N^{norm}}$		

4 Linear Transformation Is Necessary to Minimize the Warping of Space

In many biomedical applications, the bulk of the registration task can be solved by a linear transformation, requiring only a small nonlinear correction. In such cases, explicitly including both contributions into a registering transformation as done in this study, $\mathbf{T}(\mathbf{x}) = \mathbf{b} + \mathbf{A}\mathbf{x} + \mathbf{V}(\mathbf{x})$, can help minimize the warping of the space associated with $\mathbf{V}(\mathbf{x})$.

This formulation can be thought of as the Taylor series expansion of $\mathbf{T}(\mathbf{x})$ to the first order in $\mathbf{x}$, in which $\mathbf{V}(\mathbf{x})$ corresponds to the remainder term.

To illustrate this idea, fiducial points selected on a synthetic source and target image pair (Fig. 3A, B) were registered with different parameter settings, and the resulting optimal transformations were applied to the source image. The registration framework guarantees that the fiducial points register exactly, however, the type of linear transformation and parameters λ and σ can influence the warping of space. This was confirmed by analyzing the normalized deformation costs associated with linear and nonlinear parts of the registering transformations (Fig. 3C) and visually examining the registered images (Fig. 3D-G). For translation and rigid transformations, which incur no linear penalty, E_L and E_N are independent of λ since the first term in the heuristic cost of Eq. (2) is zero. For similarity and affine, there is a tradeoff between E_L and E_N, indicating that these linear transformations help reduce the cost of nonlinear distortion. Importantly, Fig. 3C shows that increasing the complexity of linear transformation results in a lower E_N, suggesting that this can help reduce space distortion. This is confirmed in Fig. 3D-G which illustrates a progressive reduction in distortion of the grid from translation to rigid to similarity to affine.

5 Registration of Traces and Images

To test the performance of the registration algorithm on biomedical data, the method was applied to a custom dataset of neuron traces and a standard dataset of retinal images.

The neuron traces were obtained from young adult hermaphrodite *C. elegans*, in which FLP neurons were fluorescently labeled with (green fluorescent protein) GFP [26] and imaged *in vivo* in 3D with a confocal microscope. Each image stack consisted of 2048 × 2048 pixels (203 × 203 μm) in the x and y dimensions and 40 z-planes (1 μm z-step). The images were traced semi-automatically in 3D using NCTracer software [27, 28] (Fig. 4A1, 2). A neuron trace captures the primary structure of a neuron as a series of points connected with line segments. Each *C. elegans* was imaged twice within 20 minutes during which time the animal was moved to a new slide to introduce nonlinear deformations. The close temporal proximity of the imaging sessions ensured minimal structural changes in neuron morphology. This process was repeated for three individual *C. elegans*, yielding three pairs of neuron traces for testing the registration.

To facilitate registration, a MATLAB graphical user interface (GUI) was developed for selecting corresponding fiducial points in source and target data. The user-selected fiducial points served as inputs to the registration algorithm, and the output transformation was subsequently applied to the entire source trace (Fig. 4A3). Registration was performed using an affine + nonlinear transformation and its accuracy was assessed by calculating the fraction of corresponding trace points between the target and registered source traces. Here, two points were deemed corresponding if their Euclidean distance was below a given threshold. Figure 4A4 shows the dependence of registration accuracy on the number of fiducial points and the threshold. It illustrates that accuracy gradually improves with the number of fiducial points, and >0.9 accuracy is achieved at an error threshold of 25 pixels with only 10 fiducial points.

Next, the performance of the registration method was tested on the Fundus Image Registration (FIRE) dataset [29] containing pairs of human retinal images acquired at

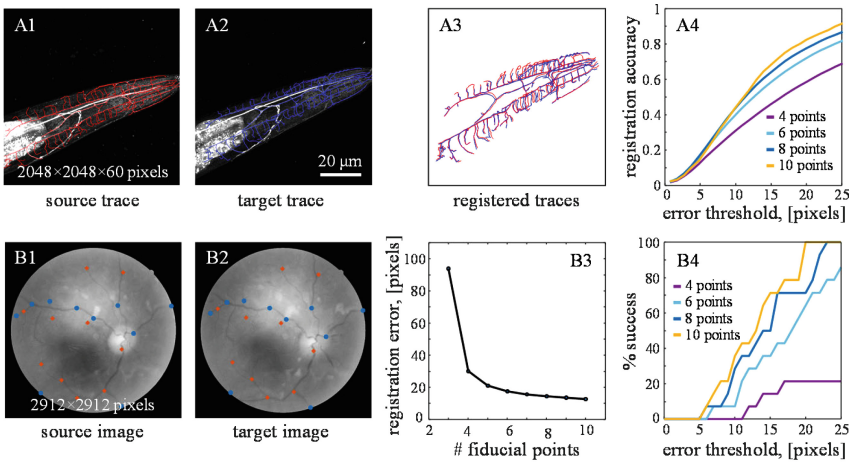

Fig. 4. Applications of the user-assisted registration method to biomedical problems. **A1.** Maximum intensity projection of a 3D image stack of an FLP neuron in *C. elegans*. The trace of its axon and dendrites (red) is used as a source for registration. **A2.** Same for the target image and trace. **A3.** Registered source and target traces from (A1) and (A2) using 10 fiducial points (affine + nonlinear, $\sigma = 100$, $\lambda = 0.5$). **A4.** Registration accuracy as a function of error threshold systematically improves with an increasing number of user-provided fiducial points ($n = 3$ neuron pairs). **B1, 2.** Sample source and target images from Category A of the FIRE dataset of retinal images, showing ground truth points (red) and user-selected fiducial points (blue). **B3.** Registration error decreases with an increasing number of fiducial points ($n = 14$ image pairs, affine + nonlinear, $\sigma = 100$, $\lambda = 0.5$). **B4.** The percentage of successfully registered image pairs as a function of the error threshold systematically increases with the number of fiducial points.

different examinations. This dataset provides ground truth points for each image pair, allowing for quantitative evaluation of registration performance. Specifically, Category A of this dataset was examined because it features 14 pairs of images containing anatomical differences due to the progression or remission of retinopathy, making it the most challenging category for registration [30]. Fiducial points for registration were selected using the GUI without prior knowledge of the ground truth points to avoid bias, and selected points within 100 pixels of a ground truth point were removed (Fig. 4B1,2).

Registration was performed using an affine + nonlinear transformation and its error was assessed by calculating the average Euclidean distance between the corresponding ground truth points on the target and registered source images. Figure 4B3 shows that this registration error decreases as more fiducial points are used for registration, and an error of <13 pixels is attained with 10 fiducial point pairs. In addition, the standard registration success rate [29] was calculated as the percentage of registered source ground truth points that were within an error threshold of their corresponding target ground truth points. Figure 4B4 shows that the user-assisted algorithm achieves a 100% registration success rate at an error threshold of 20 pixels with only 10 fiducial point pairs.

The described registration method favorably compares to the best-performing automated algorithm on the FIRE dataset [30–33] and two popular semi-automated methods (Table 3). For the comparisons with semi-automated methods, a Thin Plate Spline (TPS)

[16] implementation with the Python SciPy library [34] and B-spline-based registration implemented with SimpleITK [35] were used with the default parameters. Benchmarks were assessed based on Category A of the FIRE dataset, 10 fiducial points, and the percentage of successfully registered ground truth points at a 20-pixel threshold, as was done in Fig. 4B4.

Table 3. Registration performance of this and other methods.

Registration method	# fiducial points	% success
This method	10	100
TPS [16]	10	93.3
B-spline [35]	10	80.0
H-M 17 [30]	Automated	92.6

6 Discussion

This study describes a user-assisted registration algorithm based on an optimal combination of linear and nonlinear transformations that is accurate and efficient. By incorporating fiducial points selected by the user, the method reduces the need for iterative parameter tuning associated with fully automated algorithms, making it a practical choice for real-world applications. The versatility of this approach extends across a range of data modalities and applications. The data may involve 2D and 3D point sets, traces, and images, while the applications may include common biomedical tasks such as registration of neural traces, vascular structures, labeled tissues, and CT scans. For instance, this method can provide precise alignment of neuron traces, enabling the quantitative comparisons needed for *in vivo* longitudinal studies of structural changes associated with learning and memory formation [36–38].

Accuracy of the described registration method systematically improves with the number of fiducial points (Fig. 4) and may benefit from using a less constrained linear transformation such as similarity or affine to reduce the warping of the space (Fig. 3). However, we find that using a linear transformation that matches the registration task is the best practice for achieving robust results. In combining user input with automation, this method has the potential to achieve a balance between the accuracy and efficiency required in many registration tasks.

The registration GUI, sample images, and the dataset of neural traces used in this study are available on the Neurogeometry group GitHub site, https://github.com/neurogeometry/User-Assisted-Registration.

Acknowledgements. This work was supported by the NIH grant R56 NS128413.

Disclosure of Interests. The authors have no competing interests to declare that are relevant to the content of this article.

References

1. Holland, D., Dale, A.M., Alzheimer's Disease Neuroimaging Initiative: Nonlinear registration of longitudinal images and measurement of change in regions of interest. Med. Image Anal. **15**, 489–497 (2011)
2. Kahaki, S.M., Wang, S.-L., Stepanyants, A: Accurate registration of in vivo time-lapse images. In: Medical Imaging 2019: Image Processing, pp. 345–350. SPIE (2019)
3. Ghosh, S.S., Kakunoori, S., Augustinack, J., Nieto-Castanon, A., Kovelman, I., Gaab, N., Christodoulou, J.A., Triantafyllou, C., Gabrieli, J.D., Fischl, B.: Evaluating the validity of volume-based and surface-based brain image registration for developmental cognitive neuroscience studies in children 4 to 11 years of age. NeuroImage. **53**, 85–93 (2010)
4. Hu, Y., Modat, M., Gibson, E., Li, W., Ghavami, N., Bonmati, E., Wang, G., Bandula, S., Moore, C.M., Emberton, M.: Weakly-supervised convolutional neural networks for multimodal image registration. Med. Image Anal. **49**, 1–13 (2018)
5. Pielawski, N., Wetzer, E., Öfverstedt, J., Lu, J., Wählby, C., Lindblad, J., Sladoje, N.: CoMIR: contrastive multimodal image representation for registration. Adv. Neural Inf. Proces. Syst. **33**, 18433–18444 (2020)
6. Salvi, J., Matabosch, C., Fofi, D., Forest, J.: A review of recent range image registration methods with accuracy evaluation. Image Vis. Comput. **25**, 578–596 (2007)
7. Hoff, W.A., Nguyen, K., Lyon, T.: Computer-vision-based registration techniques for augmented reality. In: Intelligent Robots and Computer Vision XV: Algorithms, Techniques, Active Vision, and Materials Handling, pp. 538–548. SPIE (1996)
8. Sorzano, C.O.S., Thévenaz, P., Unser, M.: Elastic registration of biological images using vector-spline regularization. IEEE Trans. Biomed. Eng. **52**, 652–663 (2005)
9. Pluim, J.P., Maintz, J.A., Viergever, M.A.: Mutual-information-based registration of medical images: a survey. IEEE Trans. Med. Imaging. **22**, 986–1004 (2003)
10. Maurer, C.R., Fitzpatrick, J.M.: A review of medical image registration. In: Interactive Image-Guided Neurosurgery, vol. 1, pp. 17–44. American Association of Neurological Surgeons, Park Ridge, IL (1993)
11. Hansen, L., Heinrich, M.P.: Tackling the problem of large deformations in deep learning based medical image registration using displacement embeddings. arXiv preprint arXiv:2005.13338 (2020)
12. Myronenko, A., Song, X.: Point set registration: coherent point drift. IEEE Trans. Pattern Anal. Mach. Intell. **32**, 2262–2275 (2010)
13. Myronenko, A., Song, X., Carreira-Perpinan, M.: Non-rigid point set registration: coherent point drift. Adv. Neural Inf. Proces. Syst. **19** (2006)
14. Hirose, O.: A Bayesian formulation of coherent point drift. IEEE Trans. Pattern Anal. Mach. Intell. **43**, 2269–2286 (2020)
15. Kikinis, R., Pieper, S.D., Vosburgh, K.G.: 3D Slicer: a platform for subject-specific image analysis, visualization, and clinical support. In: Intraoperative Imaging and Image-Guided Therapy, pp. 277–289. Springer, Berlin (2013)
16. Bookstein, F.L.: Principal warps: thin-plate splines and the decomposition of deformations. IEEE Trans. Pattern Anal. Mach. Intell. **11**, 567–585 (1989)
17. Arganda-Carreras, I., Sorzano, C.O., Marabini, R., Carazo, J.M., Ortiz-de-Solorzano, C., Kybic, J.: Consistent and elastic registration of histological sections using vector-spline regularization. In: Computer Vision Approaches to Medical Image Analysis: Second International ECCV Workshop, CVAMIA 2006 Graz, Austria, May 12, 2006 Revised Papers 2, pp. 85–95. Springer, Berlin (2006)
18. Borovec, J., Kybic, J., Arganda-Carreras, I., Sorokin, D.V., Bueno, G., Khvostikov, A.V., Bakas, S., Eric, I., Chang, C., Heldmann, S.: ANHIR: automatic non-rigid histological image registration challenge. IEEE Trans. Med. Imaging. **39**, 3042–3052 (2020)

19. Fu, Y., Lei, Y., Wang, T., Curran, W.J., Liu, T., Yang, X.: Deep learning in medical image registration: a review. Phys. Med. Biol. **65**, 20TR01 (2020)
20. Kaelbling, L.P., Littman, M.L., Moore, A.W.: Reinforcement learning: a survey. J. Artif. Intell. Res. **4**, 237–285 (1996)
21. Yi, X., Walia, E., Babyn, P.: Generative adversarial network in medical imaging: a review. Med. Image Anal. **58**, 101552 (2019)
22. Tanner, C., Ozdemir, F., Profanter, R., Vishnevsky, V., Konukoglu, E., Goksel, O.: Generative adversarial networks for MR-CT deformable image registration. arXiv preprint arXiv:1807.07349 (2018)
23. Teng, Q., Liu, Z., Song, Y., Han, K., Lu, Y.: A survey on the interpretability of deep learning in medical diagnosis. Multimedia Syst. **28**, 2335–2355 (2022)
24. Gelfand, I.M., Silverman, R.A.: Calculus of Variations. Courier Corporation, Chelmsford (2000)
25. Arun, K.S., Huang, T.S., Blostein, S.D.: Least-squares fitting of two 3-D point sets. IEEE Trans. Pattern Anal. Mach. Intell. **9**(5), 698–700 (1987)
26. Chalfie, M., Tu, Y., Euskirchen, G., Ward, W.W., Prasher, D.C.: Green fluorescent protein as a marker for gene expression. Science. **263**, 802–805 (1994)
27. Chothani, P., Mehta, V., Stepanyants, A.: Automated tracing of neurites from light microscopy stacks of images. Neuroinformatics. **9**, 263–278 (2011)
28. Gala, R., Chapeton, J., Jitesh, J., Bhavsar, C., Stepanyants, A.: Active learning of neuron morphology for accurate automated tracing of neurites. Front. Neuroanat. **8**, 37 (2014)
29. Hernandez-Matas, C., Zabulis, X., Triantafyllou, A., Anyfanti, P., Douma, S., Argyros, A.A.: FIRE: fundus image registration dataset. Model. Artif. Intell. Ophthalmol. **1**, 16–28 (2017)
30. Hernandez-Matas, C., Zabulis, X., Argyros, A.A.: REMPE: registration of retinal images through eye modelling and pose estimation. IEEE J. Biomed. Health Inform. **24**, 3362–3373 (2020)
31. Chen, J., Tian, J., Lee, N., Zheng, J., Smith, R.T., Laine, A.F.: A partial intensity invariant feature descriptor for multimodal retinal image registration. IEEE Trans. Biomed. Eng. **57**, 1707–1718 (2010)
32. Yang, G., Stewart, C.V., Sofka, M., Tsai, C.-L.: Registration of challenging image pairs: initialization, estimation, and decision. IEEE Trans. Pattern Anal. Mach. Intell. **29**, 1973–1989 (2007)
33. Hernandez-Matas, C., Zabulis, X., Argyros, A.A.: Retinal image registration through simultaneous camera pose and eye shape estimation. In: 2016 38th Annual International Conference of the IEEE Engineering in Medicine and Biology Society (EMBC), pp. 3247–3251. IEEE, Piscataway (2016)
34. Virtanen, P., Gommers, R., Oliphant, T.E., Haberland, M., Reddy, T., Cournapeau, D., Burovski, E., Peterson, P., Weckesser, W., Bright, J.: SciPy 1.0: fundamental algorithms for scientific computing in Python. Nat. Methods. **17**, 261–272 (2020)
35. Beare, R., Lowekamp, B., Yaniv, Z.: Image segmentation, registration and characterization in R with SimpleITK. J. Stat. Softw. **86**, 1–35 (2018)
36. Gala, R., Lebrecht, D., Sahlender, D.A., Jorstad, A., Knott, G., Holtmaat, A., Stepanyants, A.: Computer assisted detection of axonal bouton structural plasticity in in vivo time-lapse images. elife. **6**, e29315 (2017)
37. Holtmaat, A., Svoboda, K.: Experience-dependent structural synaptic plasticity in the mammalian brain. Nat. Rev. Neurosci. **10**, 647–658 (2009)
38. Trachtenberg, J.T., Chen, B.E., Knott, G.W., Feng, G., Sanes, J.R., Welker, E., Svoboda, K.: Long-term in vivo imaging of experience-dependent synaptic plasticity in adult cortex. Nature. **420**, 788–794 (2002)